Neutron matter with chiral EFT interactions: Perturbative and first QMC calculations

I. Tews[a,b], T. Krüger[a,b], A. Gezerlis[c,a,b], K. Hebeler[a,b] and A. Schwenk[b,a]

[a] *Institut für Kernphysik, Technische Universität Darmstadt, 64289 Darmstadt, Germany*
[b] *ExtreMe Matter Institute EMMI, GSI Helmholtzzentrum für Schwerionenforschung GmbH, 64291 Darmstadt, Germany*
[c] *Department of Physics, University of Guelph, Guelph, Ontario N1G 2W1, Canada*

Abstract

Neutron matter presents a unique system in chiral effective field theory (EFT), because all many-body forces among neutrons are predicted to next-to-next-to-next-to-leading order (N^3LO). We discuss perturbative and first Quantum Monte Carlo (QMC) calculations of neutron matter with chiral EFT interactions and their astrophysical impact for the equation of state and neutron stars.

Keywords: *Chiral EFT; three-body forces; QMC; neutron matter; neutron stars*

1 Chiral EFT and many-body forces

Chiral EFT describes the interactions between nucleons at momentum scales of the order of the pion mass $Q \sim m_\pi$ based on the symmetries of QCD [1, 2]. The resulting nuclear forces are organized in a systematic expansion in powers of Q/Λ_b, where $\Lambda_b \sim 500\,\mathrm{MeV}$ denotes the breakdown scale, leading to a typical expansion parameter $Q/\Lambda_b \sim 1/3$ for nuclei. At a given order this includes contributions from one- or multi-pion exchanges that govern the long- and intermediate-range parts and from short-range contact interactions. The short-range couplings are fit to few-body data and thus capture all short-range effects relevant at low energies.

In particular, chiral EFT provides a systematic basis to investigate many-body forces and their impact on few- and many-body systems [3]. In addition, it is possible to estimate theoretical uncertainties in the EFT. An important feature of chiral EFT is the consistency of two-nucleon (NN) and three-nucleon ($3N$) interactions. This predicts the two-pion-exchange parts of the leading (N^2LO) $3N$ forces, leaving only two low-energy couplings c_D, c_E that encode pion interactions with short-range NN pairs and short-range three-body physics. At the next-order, all many-body interactions are predicted parameter-free with many new structures [1]. This makes the application of N^3LO $3N$ and $4N$ forces very exciting. This is especially the case, because $3N$ forces have been found to be key for neutron matter [4] and for neutron-rich nuclei [3, 5], see, e.g., the recent work on the calcium isotopes [6–10].

2 Neutron matter from chiral EFT interactions

The physics of neutron matter ranges from universal properties at low densities [11,12] to the densest matter in neutron stars. For neutrons, the c_D, c_E parts of N^2LO $3N$ forces do not contribute due to the Pauli principle and the pion coupling to the

Proceedings of International Conference 'Nuclear Theory in the Supercomputing Era — 2013' (NTSE-2013), Ames, IA, USA, May 13–17, 2013. Eds. A. M. Shirokov and A. I. Mazur. Pacific National University, Khabarovsk, Russia, 2014, p. 302.
http://www.ntse-2013.khb.ru/Proc/Schwenk.pdf.

nucleon spin (also the c_4 two-pion-exchange part does not contribute due to the isospin structure) [4]. Therefore, all three- and four-neutron forces are predicted to N^{3}LO. To study these, we recently presented the first calculation of the neutron-matter energy that includes all NN, $3N$, and $4N$ interactions consistently to N^{3}LO [13, 14].

The largest contributions to the neutron-matter energy arise from NN interactions. In Refs. [13,14] we studied the perturbative convergence of all existing NN potentials at N^{2}LO and at N^{3}LO of Epelbaum, Glöckle, and Meißner (EGM) [15,16] with cutoffs $\Lambda/\tilde{\Lambda} = 450/500, 450/700, 550/600, 600/600$, and $600/700$ MeV, where Λ and $\tilde{\Lambda}$ denote the cutoff in the Lippmann–Schwinger equation and in the two-pion-exchange spectral-function regularization, respectively; as well as the available N^{3}LO NN potentials of Entem and Machleidt (EM) [2, 17] with cutoffs $\Lambda = 500$ and 600 MeV.

To study the perturbative convergence of the different NN potentials, we calculated the Hartree–Fock as well as second- and third-order energies, only including particle-particle diagrams, with both free and Hartree–Fock single-particle energies. The results for NN and N^{2}LO $3N$ forces are shown in Fig. 1 for the perturbative NN

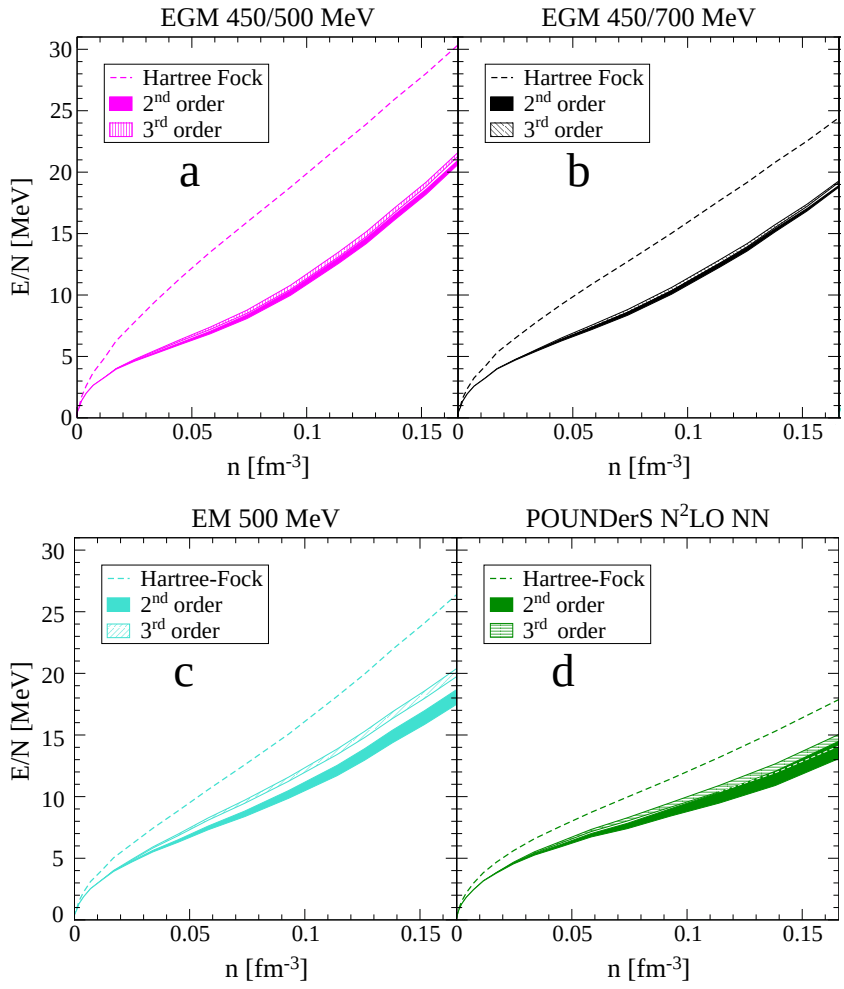

Figure 1: Panels a–c: Neutron-matter energy per particle E/N as a function of density n for the N^{3}LO NN potentials that exhibit a perturbative convergence. The dashed lines are Hartree–Fock results. The filled and shaded bands are second- and third-order results, where at each order the band ranges from using a free to a Hartree–Fock spectrum. All calculations include N^{2}LO $3N$ forces with a $3N$ cutoff $\Lambda = 2.0\,\mathrm{fm}^{-1}$ and low-energy couplings $c_1 = 0.75\,\mathrm{GeV}^{-1}$ and $c_3 = 4.77\,\mathrm{GeV}^{-1}$. For details see Ref. [14]. Panel d: Same for the POUNDerS N^{2}LO NN potential (without $3N$ forces).

interactions for a $3N$ cutoff $\Lambda = 2.0\,\mathrm{fm}^{-1}$ and a particular choice of $c_1 = 0.75\,\mathrm{GeV}^{-1}$, $c_3 = 4.77\,\mathrm{GeV}^{-1}$, although the general picture is unchanged for other coupling values. The bands result from using a free to a Hartree–Fock single-particle spectrum. The N^{3}LO EGM potentials with cutoffs 450/500 MeV and 450/700 MeV exhibit only small energy changes from second to third order. This indicates that these potentials are perturbative for neutron matter. For the EM 500 MeV potential the difference between second and third order is larger compared to the EGM potentials. Since this potential is most commonly used in nuclear structure calculations, we include it in our complete N^{3}LO calculation. The perturbative convergence for these potentials in neutron matter is similar to renormalization-group-evolved interactions in nuclear matter [18]. We have also studied in Fig. 1 the POUNDerS N^{2}LO NN potential [19], which is found to be perturbative as well. In addition, there are in-medium chiral perturbation theory schemes that treat the Fermi momentum as an explicit scale [20,21].

The larger-cutoff N^{3}LO EGM 550/600 MeV and 600/600 MeV potentials as well as the EM 600 MeV potential are not used in our calculations because they show large changes from second to third order [14]. This demonstrates that these interactions are nonperturbative. The N^{3}LO EGM 600/600 MeV potential is not used because it breaks Wigner symmetry ($C_T = 0$) at the interaction level (as discussed in Ref. [14]).

The subleading N^{3}LO $3N$ forces have been derived recently [22, 23]. They can be grouped into five topologies, where the latter two depend on the NN contacts $C_{T/S}$:

$$V_{3N}^{\mathrm{N^3LO}} = V^{2\pi} + V^{2\pi\text{-}1\pi} + V^{\mathrm{ring}} + V^{2\pi\text{-cont}} + V^{1/m}. \tag{1}$$

$V^{2\pi}$, $V^{2\pi\text{-}1\pi}$, and V^{ring} denote the long-range two-pion-exchange, the two-pion–one-pion-exchange, and the pion-ring $3N$ interactions, respectively [22]. The terms $V^{2\pi\text{-cont}}$ and $V^{1/m}$ are the short-range two-pion-exchange–contact $3N$ interaction and $3N$ relativistic corrections [23]. The N^{3}LO $4N$ forces have been derived in Refs. [24, 25] and in general depend on the contact C_T, but in neutron matter the C_T-dependent parts do not contribute. There are seven $4N$ topologies that lead to non-vanishing contributions. In neutron matter only two three-pion-exchange diagrams (in Ref. [24] named V^a and V^e) and the pion-pion-interaction diagram (V^f) contribute [13].

The N^{3}LO many-body interactions are evaluated in the Hartree–Fock approximation, which is expected to be reliable for neutron matter [4]. We show the individual contributions of the $3N$ and $4N$ forces in Fig. 2, where the bands correspond to the $3N/4N$ cutoff variation $\Lambda = 2\text{–}2.5\,\mathrm{fm}^{-1}$. The N^{3}LO two-pion-exchange expectation value (panel 1) sets the expected scale of N^{3}LO $3N$ interactions. Compared to this, we find relatively large expectation values in the $V^{2\pi\text{-}1\pi}$, V^{ring}, and $V^{2\pi\text{-cont}}$ topologies. This could indicate that in these topologies Δ contributions shifted to N^{4}LO are expected to be important [14, 26]. The $3N$ relativistic corrections and the contributions from N^{3}LO $4N$ forces are small (see also Ref. [27]). However, also for $4N$ forces additional larger contributions from Δ excitations may arise at N^{4}LO [28].

The complete N^{3}LO result for neutron matter is shown in the left panel of Fig. 3, which includes all NN, $3N$, and $4N$ interactions to N^{3}LO [13]. At saturation density, we obtain for the energy per particle $E/N = 14.1\text{–}21.0\,\mathrm{MeV}$. This range is based on different NN potentials, a variation of the couplings $c_1 = -(0.75\text{–}1.13)\,\mathrm{GeV}^{-1}$, $c_3 = -(4.77\text{–}5.51)\,\mathrm{GeV}^{-1}$ [26], which dominates the total uncertainty, a $3N/4N$-cutoff variation $\Lambda = 2\text{–}2.5\,\mathrm{fm}^{-1}$, and the uncertainty in the many-body calculation.

The neutron-matter energy in Fig. 3 is in very good agreement with NLO lattice results [29] and QMC simulations [12] at very low densities (see also the inset). At nuclear densities, we compare our N^{3}LO results with variational calculations based on phenomenological potentials (APR) [30], which are within the N^{3}LO band, but do not provide theoretical uncertainties. In addition, we compare the density dependence with results from Auxiliary Field Diffusion MC (AFDMC) calculations (GCR) [31] based on nuclear force models adjusted to a symmetry energy of 32 MeV.

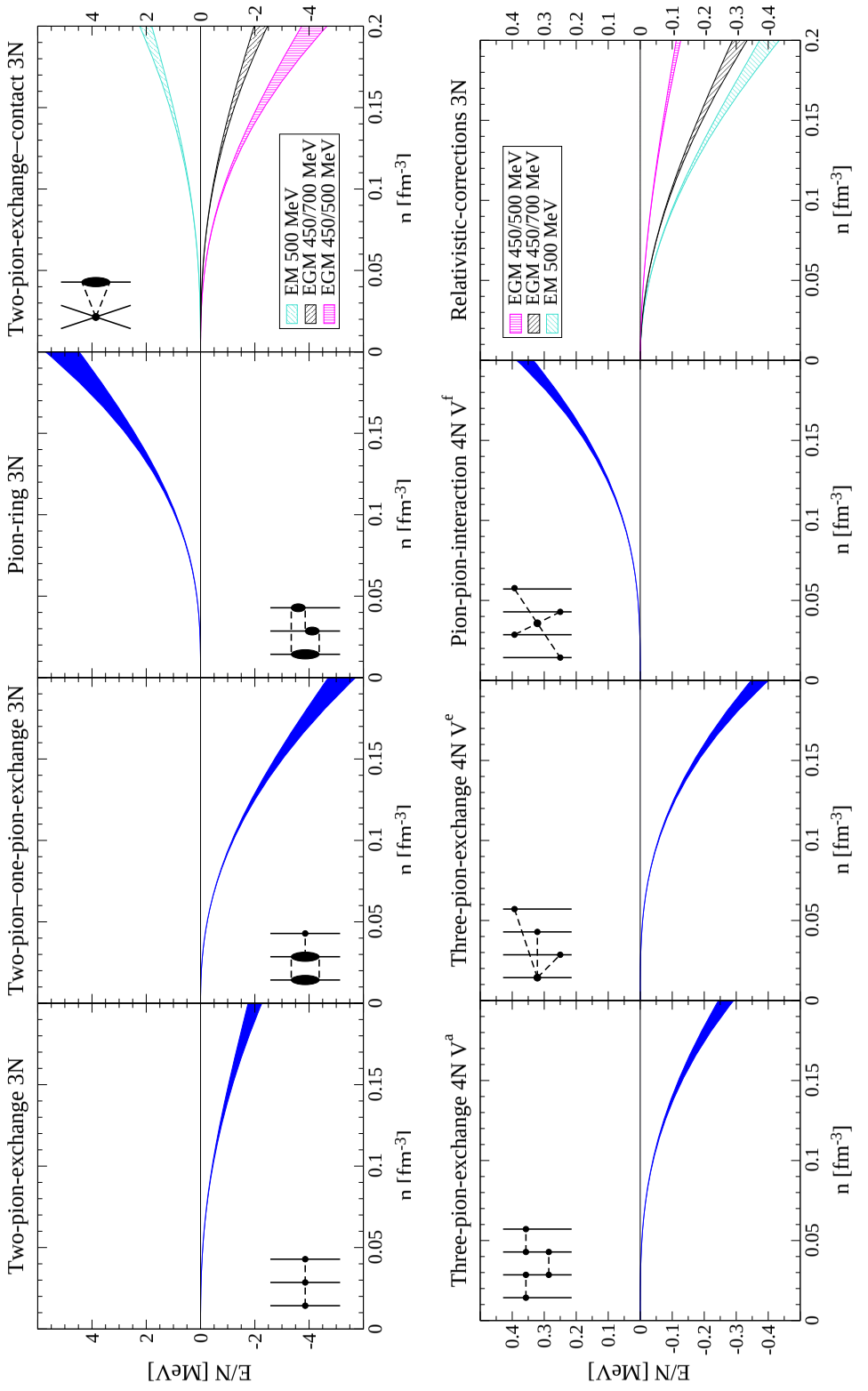

Figure 2: Energy per particle E/N as a function of density n for all individual N^{3}LO $3N$- and $4N$-force contributions to neutron matter at the Hartree–Fock level [13]. All bands are obtained by varying the $3N/4N$ cutoffs $\Lambda = 2.0{-}2.5\,\mathrm{fm}^{-1}$. For the $3N$ two-pion-exchange–contact forces and the $3N$ relativistic corrections, the different bands correspond to the different NN contacts, C_T and C_S, determined consistently for the N^{3}LO EM/EGM potentials. The diagrams illustrate the $3N/4N$ force topology.

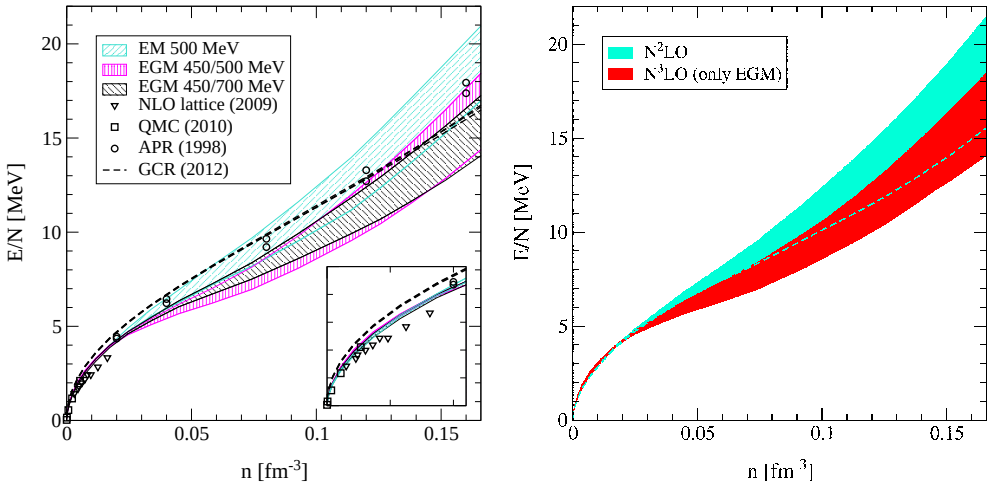

Figure 3: Left panel: Neutron-matter energy per particle E/N as a function of density n including NN, $3N$ and $4N$ forces to N^{3}LO for the given EM/EGM NN potentials [13]. The bands include uncertainty estimates due to the many-body calculation, the low-energy c_i couplings, and by varying the $3N/4N$ cutoffs. For comparison, results are shown at low densities (see also the inset) from NLO lattice [29] and QMC simulations [12], and at nuclear densities from variational [30] and Auxiliary Field Diffusion MC calculations (GCR) [31] based on phenomenological potentials. Right panel: Neutron-matter energy per particle at N^{2}LO (upper cyan band that extends to the dashed line) and N^{3}LO (lower red band) [13]. The bands are based on the EGM NN potentials and include the same uncertainty estimates.

We also compare the convergence from N^{2}LO to N^{3}LO in the same calculational setup. For this comparison, we only consider the EGM potentials with cutoffs 450/500 MeV and 450/700 MeV. This leads to an N^{3}LO energy range of 14.1−18.4 MeV per particle at n_0. For the N^{2}LO band in the right panel of Fig. 3, we have estimated the theoretical uncertainties in the same way, and find an energy of 15.5−21.4 MeV per particle at n_0. The two bands overlap but the range of the band is only reduced by a factor of 2/3 in contrast to the 1/3 expected from the EFT power counting. We attribute this to Δ effects (see the discussion in Refs. [13, 14]).

3 QMC calculations with chiral EFT interactions

Quantum Monte Carlo methods have not been used with chiral EFT interactions due to nonlocalities in their present implementation in momentum space. Nonlocalities are difficult to handle in QMC [32]. In the momentum-space interactions, there are two sources of nonlocalities: first, due to regulator functions that lead to nonlocal interactions upon Fourier transformation, and second, due to contact interactions that depend on the momentum transfer in the exchange channel $\mathbf{k}$ and from $\mathbf{k}$-dependent parts in pion-exchange contributions beyond N^{2}LO. For applications in QMC, we have developed local chiral EFT interactions in Ref. [32].

To avoid regulator-generated nonlocalities for the long-range pion-exchange parts, we use the local coordinate-space expressions for the LO one-pion-exchange as well as NLO and N^{2}LO two-pion-exchange interactions [33,34] and regulate them directly in coordinate space using the function $f_{\rm long}(r) = 1 - e^{-(r/R_0)^4}$, which smoothly cuts off interactions at short distances $r < R_0$ while leaving the long-range parts unchanged [32]. So, R_0 takes over the role of the cutoff Λ in momentum space.

To remove the $\mathbf{k}$-dependent contact interactions to N^{2}LO, we make use of the

freedom to choose a basis of short-range operators in chiral EFT interactions (similar to Fierz ambiguities). At LO, one usually considers the two momentum-independent contact interactions $C_S + C_T\,\boldsymbol{\sigma}_1\cdot\boldsymbol{\sigma}_2$. However, it is equivalent to choose any two of the four operators $\mathbb{1}$, $\boldsymbol{\sigma}_1\cdot\boldsymbol{\sigma}_2$, $\boldsymbol{\tau}_1\cdot\boldsymbol{\tau}_2$, and $\boldsymbol{\sigma}_1\cdot\boldsymbol{\sigma}_2\,\boldsymbol{\tau}_1\cdot\boldsymbol{\tau}_2$, with spin and isospin operators $\boldsymbol{\sigma}_i, \boldsymbol{\tau}_i$, because there are only two S-wave channels due to the Pauli principle. It is a convention in present chiral EFT interactions to neglect the isospin dependence, which is then generated from the exchange terms [15–17].

We use this freedom to keep at NLO (order Q^2) an isospin-dependent q^2 contact interaction and an isospin-dependent $(\boldsymbol{\sigma}_1\cdot\mathbf{q})(\boldsymbol{\sigma}_2\cdot\mathbf{q})$ tensor part in favor of a nonlocal k^2 contact interaction and a nonlocal $(\boldsymbol{\sigma}_1\cdot\mathbf{k})(\boldsymbol{\sigma}_2\cdot\mathbf{k})$ tensor part. This leads to the following seven linearly independent contact interactions at NLO that are local [32],

$$V_{\rm short}^{\rm NLO} = C_1\,q^2 + C_2\,q^2\,\boldsymbol{\tau}_1\cdot\boldsymbol{\tau}_2 + \big(C_3\,q^2 + C_4\,q^2\,\boldsymbol{\tau}_1\cdot\boldsymbol{\tau}_2\big)\,\boldsymbol{\sigma}_1\cdot\boldsymbol{\sigma}_2 + i\,\frac{C_5}{2}\,(\boldsymbol{\sigma}_1+\boldsymbol{\sigma}_2)\cdot\mathbf{q}\times\mathbf{k} + C_6\,(\boldsymbol{\sigma}_1\cdot\mathbf{q})(\boldsymbol{\sigma}_2\cdot\mathbf{q}) + C_7\,(\boldsymbol{\sigma}_1\cdot\mathbf{q})(\boldsymbol{\sigma}_2\cdot\mathbf{q})\,\boldsymbol{\tau}_1\cdot\boldsymbol{\tau}_2, \quad (2)$$

where the only $\mathbf{k}$-dependent contact interaction (C_5) is a spin-orbit potential.

The low-energy couplings $C_{S/T}$ at LO plus C_{1-7} at NLO and N^{2}LO are fitted in Ref. [36] for different R_0 to the NN phase shifts of the Nijmegen partial-wave analysis [35] at laboratory energies $E_{\rm lab} = 1, 5, 10, 25, 50$, and 100 MeV, using a local regulator. The reproduction of the isospin $T = 1$ S- and P-waves is shown order by order in Fig. 4, where the bands are obtained by varying R_0 between 0.8−1.2 fm and provide a measure of the theoretical uncertainty. At N^{2}LO, an isospin-symmetry-breaking contact interaction (C_{nn} for neutrons) is added, which is fitted to $a_{nn} = -18.8$ fm. As shown in Fig. 4, the comparison with NN phase shifts is very good for $E_{\rm lab} \lesssim 150$ MeV. This is similar for higher partial waves and isospin $T = 0$ channels. In cases where there are deviations for higher energies (such as in the $^3P_2$), the width of the band signals significant theoretical uncertainties due to the chiral EFT truncation at N^{2}LO. The NLO and N^{2}LO bands nicely overlap or are very close, but it is also apparent that the bands at N^{2}LO are of a similar size as at NLO. This is because the width of the bands at both NLO and N^{2}LO shows effects of the neglected order-Q^4 contact interactions.

Since nuclear forces contain quadratic spin, isospin, and tensor operators (of the form $\boldsymbol{\sigma}_i^\alpha\,A_{ij}^{\alpha\beta}\,\boldsymbol{\sigma}_j^\beta$), the many-body wave function cannot be expressed as a product of single-particle spin-isospin states. All possible spin-isospin nucleon-pair states need to be explicitly accounted for, leading to an exponential increase in the number of possible states. However, the AFDMC method [37] is capable of efficiently handling spin-dependent Hamiltonians. AFDMC rewrites the Green's function by applying a Hubbard–Stratonovich transformation using auxiliary fields to change the quadratic spin-isospin operator dependences to linear. For the case of neutrons, it is also possible to include spin-orbit interactions and $3N$ forces in AFDMC nonperturbatively [38,39].

In the upper panel of Fig. 5 we show first AFDMC calculations for the neutron-matter energy with local chiral EFT NN interactions at LO, NLO, and N^{2}LO [32]. At each order, the full interaction is used both in the propagator and when evaluating observables. The bands in Fig. 5 give the range of the energy obtained by varying R_0 between 0.8−1.2 fm, where the softer $R_0 = 1.2$ fm interactions yield the lower energies. At LO, the energy has a large uncertainty. The overlap of the bands at different orders in Fig. 5 is very systematic. In addition, the result that the NLO and N^{2}LO bands are comparable is expected from the discussion of the phase-shift bands in Fig. 4 and from the large c_i entering at N^{2}LO.

Our AFDMC results provide first nonperturbative benchmarks for chiral EFT interactions at nuclear densities. We have performed perturbative calculations as in the previous section based on the same local N^{2}LO NN interactions. The perturbative energies are compared in the lower panel of Fig. 5 to the AFDMC N^{2}LO results. For the softer $R_0 = 1.2$ fm ($\Lambda \sim 400$ MeV) interaction, the third-order corrections

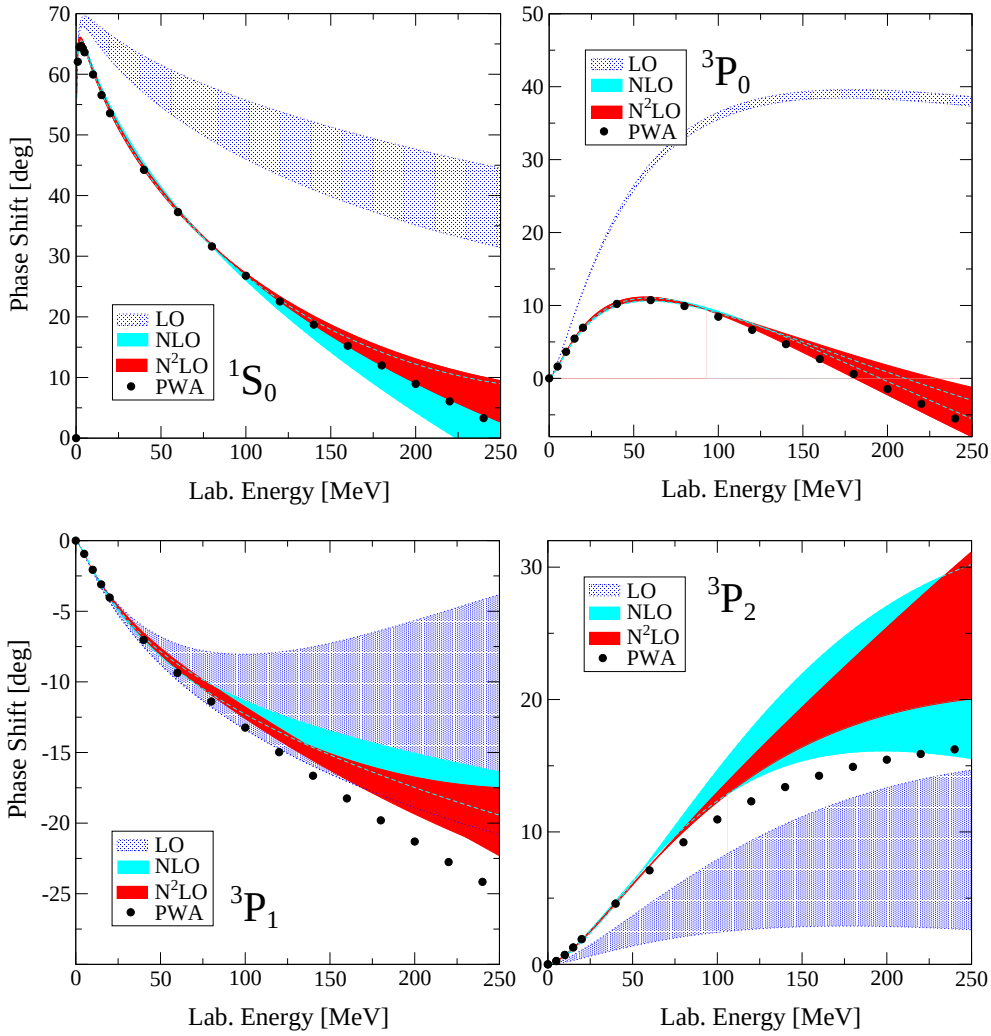

Figure 4: Neutron-proton phase shifts as a function of laboratory energy in the ${}^1S_0$, ${}^3P_0$, ${}^3P_1$, and ${}^3P_2$ partial waves in comparison to the Nijmegen partial-wave analysis (PWA) [35]. The LO, NLO, and N^{2}LO local chiral potential bands are obtained by varying R_0 between 0.8−1.2 fm (with a spectral-function cutoff $\widetilde{\Lambda} = 800$ MeV) [32,36].

are small and the perturbative third-order energy is in excellent agreement with the AFDMC results, while for the harder $R_0 = 0.8$ fm ($\Lambda \sim 600$ MeV) interaction, the convergence is clearly slow. This is the first nonperturbative validation for neutron matter of the possible perturbativeness of low-cutoff $\Lambda \sim 400$ MeV interactions [40].

4 Astrophysical applications

The symmetry energy S_v and its density derivative L provide important input for astrophysics [41]. To calculate these, we follow Ref. [42]. The predicted ranges for S_v and L at saturation density are $S_v = 28.9$−34.9 MeV and $L = 43.0$−66.6 MeV. The S_v and L ranges are in very good agreement with experimental constraints from nuclear masses [43] and from the dipole polarizability of ^{208}Pb [44], see the left panel of Fig. 6. In addition, they also overlap with the results for RG-evolved NN interactions with N^{2}LO $3N$ forces [41, 42], but due to the additional density dependences from N^{3}LO

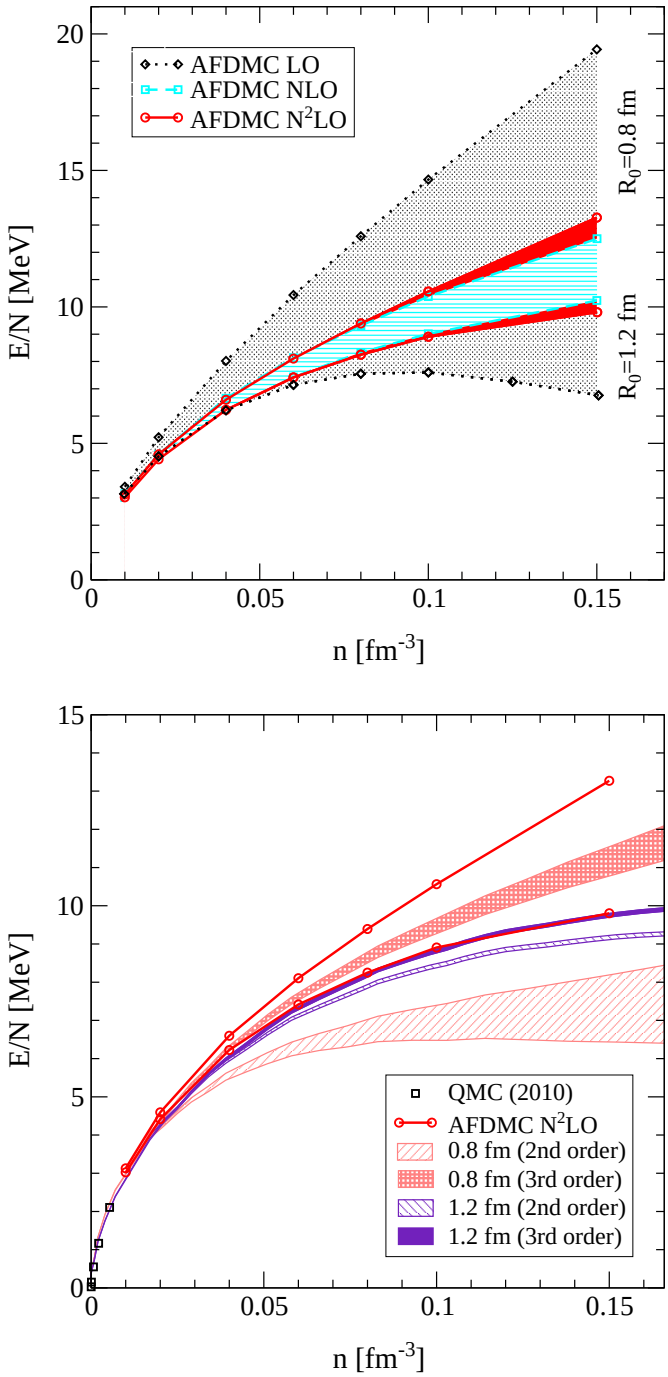

Figure 5: Upper panel: Neutron-matter energy per particle E/N as a function of density n calculated using AFDMC with chiral EFT NN interactions at LO, NLO, and N^{2}LO [32]. The statistical errors are smaller than the points shown. The lines give the range obtained by varying R_0 between 0.8−1.2 fm. Lower panel: The AFDMC N^{2}LO band in comparison to perturbative calculations using the same N^{2}LO NN interactions. The lower (upper) limit of the AFDMC N^{2}LO band is for $R_0 = 1.2$ fm ($R_0 = 0.8$ fm), corresponding to a momentum cutoff $\Lambda \sim 400$ MeV ($\Lambda \sim 600$ MeV). Perturbative results are shown at second and third order. For the softer $R_0 = 1.2$ fm interaction (narrow purple bands), third-order corrections are small and the third-order energy is in excellent agreement with the AFDMC results, while for the harder $R_0 = 0.8$ fm interaction (light red bands), the convergence is clearly slow.

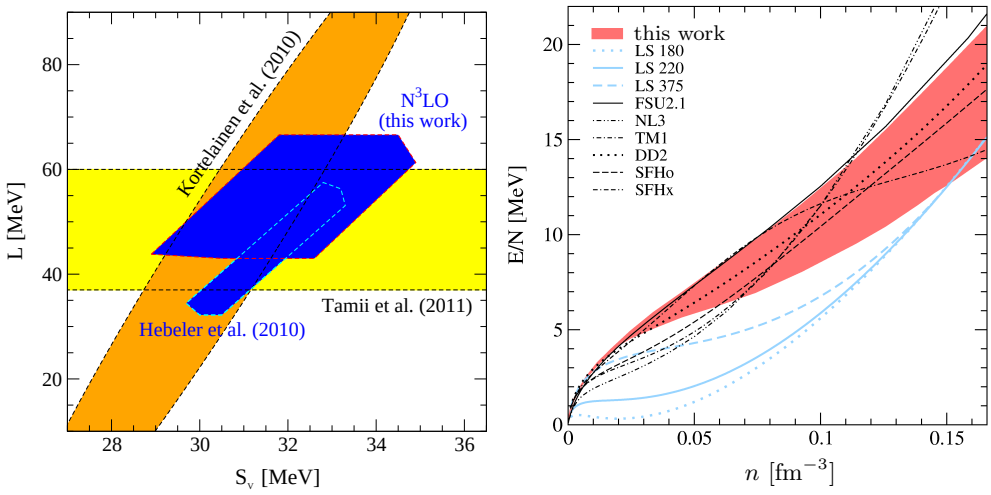

Figure 6: Left panel: Range for the symmetry energy S_v and its density dependence L obtained at N^{3}LO [13] versus including $3N$ forces at N^{2}LO (Hebeler *et al.* [42]). For comparison, see Ref. [41], we show constraints obtained from energy-density functionals for nuclear masses (Kortelainen *et al.* [43]) and from the ^{208}Pb dipole polarizability (Tamii *et al.* [44]). Right panel: Comparison of the N^{3}LO neutron-matter energy of the left panel of Fig. 3 (red band) with equations of state for core-collapse supernova simulations provided by Lattimer–Swesty (LS with different incompressibilities 180, 220, and 375 MeV), G. Shen (FSU2.1, NL3), Hempel (TM1, SFHo, SFHx), and Typel (DD2). For details see Ref. [14].

many-body forces, the correlation between S_v and L is not as tight.

The neutron-matter results also provide constraints for equations of state for core-collapse-supernova simulations. In the right panel of Fig. 6, we compare the N^{3}LO neutron-matter band (red band) to the Lattimer–Swesty (LS) equation of state [45] (with different incompressibilities 180, 220, and 375 MeV), which is most commonly used in simulations, and to different relativistic mean-field-theory equations of state based on the density functionals DD2 [46], FSU2.1 [47], NL3 [48], SFHo, SFHx [49], and TM1 [50]. At low densities only the DD2, FSU2.1 and SFHx equations of state are consistent with the N^{3}LO neutron-matter band. The NL3 and TM1 equations of state have a too strong density dependence, which leads to unnaturally large S_v and L values. In addition, Fig. 6 exhibits a strange density dependence of SFHx.

Next, we use the N^{3}LO neutron-matter results to provide constraints for the structure of neutron stars. We follow Refs. [42, 51] for incorporating beta equilibrium and for the extension to high densities using piecewise polytropes that are constrained by causality and by the requirement to support a $1.97 \pm 0.04\,M_\odot$ neutron star [52] (see also the recent $2.01 \pm 0.04\,M_\odot$ discovery [53]). In addition, we consider the case, if a $2.4\,M_\odot$ neutron star were to be observed. The resulting constraints on the neutron star mass-radius diagram are shown in Fig. 7 by the red bands. The bands represent an envelope of a large number of individual equations of state reflecting the uncertainties in the N^{3}LO neutron-matter calculation and in the polytropic extensions to high densities [42, 51]. The combination with the $2\,M_\odot$ neutron star (left panel) predicts a radius range of 9.7−13.9 km for a $1.4\,M_\odot$ star [14, 42]. The maximal neutron star mass is found to be $3.1\,M_\odot$, with a corresponding radius of about 14 km. We also find very good agreement with the mass-radius constraints from the neutron-matter calculations based on RG-evolved NN interactions with N^{2}LO $3N$ forces [42], which are shown by the thick dashed blue lines in the left panel of Fig. 7.

In addition, we show in Fig. 7 the mass-radius relations obtained from equations

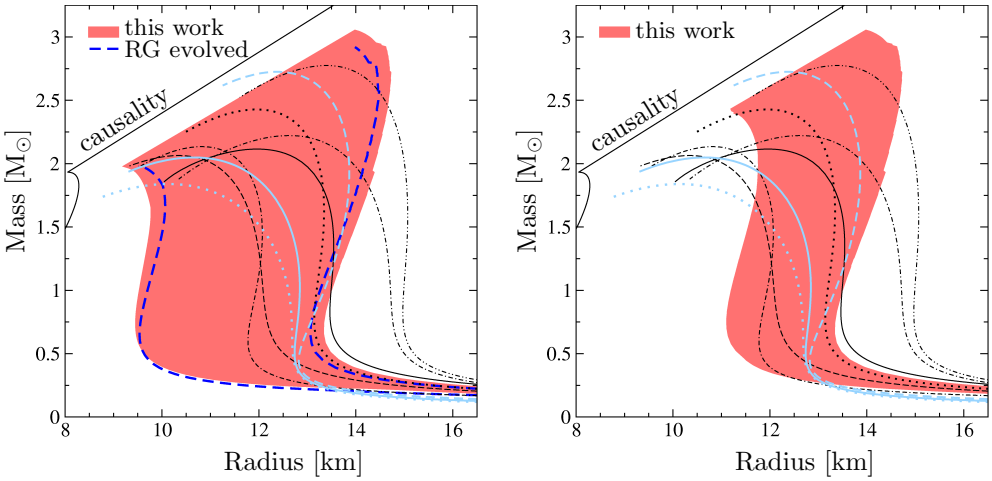

Figure 7: Constraints on the mass-radius diagram of neutron stars based on our neutron-matter results at N^{3}LO following Ref. [42, 51] for the extension to neutron-star matter and to high densities (red band), in comparison to the constraints from calculations based on RG-evolved NN interactions (thick dashed blue lines) [42]. We also show the mass-radius relations obtained from the equations of state for core-collapse supernova simulations shown in Fig. 6. Left panel: Band obtained with the constraint of a 1.97 $M_\odot$ neutron star [14]. Right panel: Same for a 2.4 $M_\odot$ star.

of state for core-collapse supernova simulations [45, 47–50, 54, 55]. The inconsistency in Fig. 6 of many of the equations of state with the N^{3}LO neutron-matter band at low densities results in a large spread of very low mass/large radius neutron stars, where the red band is considerably narrower in Fig. 7. For typical neutron stars, our calculations rule out the NL3 and TM1 equations of state, which produce too large radii. Finally, we have also explored the constraints from N^{3}LO calculations for the chiral condensate in neutron matter [56].

All the very best for your 70th birthday, James, lots of good health and energy for fun in life and physics (and many days like the one we enjoyed in Capri)! We would like to thank E. Epelbaum, S. Gandolfi, J. M. Lattimer, A. Nogga, and C. J. Pethick, who contributed to the results presented in this talk. This work was supported by the DFG through Grant SFB 634, the ERC Grant No. 307986 STRONGINT, the Helmholtz Alliance HA216/EMMI, and NSERC. Computations were performed at the Jülich Supercomputing Center and at NERSC.

References

[1] E. Epelbaum, H.-W. Hammer and U.-G. Meißner, Rev. Mod. Phys. **81**, 1773 (2009).

[2] R. Machleidt and D. R. Entem, Phys. Rept. **503**, 1 (2011).

[3] H.-W. Hammer, A. Nogga and A. Schwenk, Rev. Mod. Phys. **85**, 197 (2013).

[4] K. Hebeler and A. Schwenk, Phys. Rev. C **82**, 014314 (2010).

[5] T. Otsuka, T. Suzuki, J. D. Holt, A. Schwenk and Y. Akaishi, Phys. Rev. Lett. **105**, 032501 (2010).

[6] J. D. Holt, T. Otsuka, A. Schwenk and T. Suzuki, J. Phys. G **39**, 085111 (2012).

[7] G. Hagen, M. Hjorth-Jensen, G. R. Jansen, R. Machleidt and T. Papenbrock, Phys. Rev. Lett. **109**, 032502 (2012).

[8] A. T. Gallant *et al.*, Phys. Rev. Lett. **109**, 032506 (2012).

[9] J. D. Holt, J. Menéndez and A. Schwenk, J. Phys. G **40**, 075105 (2013).

[10] F. Wienholtz *et al.*, Nature **498**, 346 (2013).

[11] A. Schwenk and C. J. Pethick, Phys. Rev. Lett. **95**, 160401 (2005).

[12] A. Gezerlis and J. Carlson, Phys. Rev. C **81**, 025803 (2010); A. Gezerlis and R. Sharma, *ibid.* **85**, 015806 (2012).

[13] I. Tews, T. Krüger, K. Hebeler and A. Schwenk, Phys. Rev. Lett. **110**, 032504 (2013).

[14] T. Krüger, I. Tews, K. Hebeler and A. Schwenk, Phys. Rev. C **88**, 025802 (2013).

[15] E. Epelbaum, W. Glöckle and U.-G. Meißner, Eur. Phys. J. A **19**, 401 (2004).

[16] E. Epelbaum, W. Glöckle and U.-G. Meißner, Nucl. Phys. A **747**, 362 (2005).

[17] D. R. Entem and R. Machleidt, Phys. Rev. C **68**, 041001(R) (2003).

[18] S. K. Bogner, A. Schwenk, R. J. Furnstahl and A. Nogga, Nucl. Phys. A **763**, 59 (2005); K. Hebeler, S. K. Bogner, R. J. Furnstahl, A. Nogga and A. Schwenk, Phys. Rev. C **83**, 031301(R) (2011).

[19] A. Ekström, G. Baardsen, C. Forssén, G. Hagen, M. Hjorth-Jensen, G. R. Jansen, R. Machleidt, W. Nazarewicz, T. Papenbrock, J. Sarich and S. M. Wild, Phys. Rev. Lett. **110**, 192502 (2013).

[20] N. Kaiser, S. Fritsch and W. Weise, Nucl. Phys. A **697**, 255 (2002); J. W. Holt, N. Kaiser and W. Weise, arXiv:1304.6350 (2013).

[21] A. Lacour, J. A. Oller and U.-G. Meißner, Ann. Phys. (NY) **326**, 241 (2011).

[22] V. Bernard, E. Epelbaum, H. Krebs and U.-G. Meißner, Phys. Rev. C **77**, 064004 (2008).

[23] V. Bernard, E. Epelbaum, H. Krebs and U.-G. Meißner, Phys. Rev. C **84**, 054001 (2011).

[24] E. Epelbaum, Phys. Lett. B **639**, 456 (2006).

[25] E. Epelbaum, Eur. Phys. J. A **34**, 197 (2007).

[26] H. Krebs, A. Gasparyan and E. Epelbaum, Phys. Rev. C **85**, 054006 (2012).

[27] S. Fiorilla, N. Kaiser and W. Weise, Nucl. Phys. A **880**, 65 (2012).

[28] N. Kaiser, Eur. Phys. J. A **48**, 135 (2012).

[29] E. Epelbaum, H. Krebs, D. Lee and U.-G. Meißner, Eur. Phys. J. A **40**, 199 (2009).

[30] A. Akmal, V. R. Pandharipande and D. G. Ravenhall, Phys. Rev. C **58**, 1804 (1998).

[31] S. Gandolfi, J. Carlson and S. Reddy, Phys. Rev. C **85**, 032801(R) (2012).

[32] A. Gezerlis, I. Tews, E. Epelbaum, S. Gandolfi, K. Hebeler, A. Nogga and A. Schwenk, Phys. Rev. Lett. **111**, 032501 (2013).

[33] N. Kaiser, R. Brockmann and W. Weise, Nucl. Phys. A **625**, 758 (1997).

[34] E. Epelbaum, W. Glöckle and U.-G. Meißner, Eur. Phys. J. A **19**, 125 (2004).

[35] V. G. J. Stoks, R. A. M. Klomp, M. C. M. Rentmeester and J. J. de Swart, Phys. Rev. C **48**, 792 (1993).

[36] M. Freunek, *Diploma thesis.* Universität Bonn and Forschungszentrum Jülich, 2007.

[37] K. E. Schmidt and S. Fantoni, Phys. Lett. B **446**, 99 (1999).

[38] A. Sarsa, S. Fantoni, K. E. Schmidt and F. Pederiva, Phys. Rev. C **68**, 024308 (2003).

[39] S. Gandolfi, A. Yu. Illarionov, K. E. Schmidt, F. Pederiva and S. Fantoni, Phys. Rev. C **79**, 054005 (2009).

[40] S. K. Bogner, R. J. Furnstahl and A. Schwenk, Progr. Part. Nucl. Phys. **65**, 94 (2010).

[41] J. M. Lattimer and Y. Lim, Astrophys. J. **771**, 51 (2013).

[42] K. Hebeler, J. M. Lattimer, C. J. Pethick and A. Schwenk, Astrophys. J. **773**, 11 (2013).

[43] M. Kortelainen, T. Lesinski, J. Moré, W. Nazarewicz, J. Sarich, N. Schunck, M. Stoitsov and S. Wild, Phys. Rev. C **82**, 024313 (2010).

[44] A. Tamii *et al.*, Phys. Rev. Lett. **107**, 062502 (2011).

[45] J. M. Lattimer and F. D. Swesty, Nucl. Phys. A **535**, 331 (1991).

[46] S. Typel, *private communication.*

[47] G. Shen, C. J. Horowitz and E. O'Connor, Phys. Rev. C **83**, 065808 (2011).

[48] G. Shen, C. J. Horowitz and S. Teige, Phys. Rev. C **83**, 035802 (2011).

[49] A. W. Steiner, M. Hempel and T. Fischer, arXiv:1207.2184 (2012).

[50] H. Shen, H. Toki, K. Oyamatsu and K. Sumiyoshi, Astrophys. J. Suppl. **197**, 20 (2011).

[51] K. Hebeler, J. M. Lattimer, C. J. Pethick and A. Schwenk, Phys. Rev. Lett. **105**, 161102 (2010).

[52] P. B. Demorest, T. Pennucci, S. M. Ransom, M. S. E. Roberts and J. W. T. Hessels, Nature **467**, 1081 (2010).

[53] J. Antoniadis *et al.*, Science **340**, 448 (2013).

[54] M. Hempel, T. Fischer, J. Schaffner-Bielich and M. Liebendörfer, Astrophys. J. **748**, 70 (2012).

[55] E. O'Connor, *private communication*; A. Kleiner, *B. Sc. Thesis.* Technische Universität Darmstadt, 2012.

[56] T. Krüger, I. Tews, B. Friman, K. Hebeler and A. Schwenk, Phys. Lett. B **726**, 412 (2013).